Chapter 6

CONSTANT STRESS AND PRESSURE RHEOLOGY OF COLLOIDAL SUSPENSIONS

[1] M. Wang and J. F. Brady, "Constant stress and pressure rheology of colloidal suspensions", Physical Review Letters **115**, 158301 (2015) doi:10.1103/PhysRevLett.115.158301,

6.1 Introduction

Amorphous materials such as metallic glasses, granular matter, and colloidal suspensions exhibit a range of flow behaviors including shear-thickening [1], particle migration [2], shear banding [3], *etc*. The most fundamental and universal aspect of their rheology is a flow-arrest transition that takes place at either increased density or reduced temperature and is summarized by various 'jamming diagrams', pioneered by Liu & Nagel [4–6]. Extensive computational and experimental investigations reveal that the flow-arrest transition is affected by the interplay among thermal fluctuations [6–10] and particle geometry and interactions [11–14]. Distinct behaviors have been observed for strong and weak thermal fluctuations, but the connection between the two limits is an open question.

In this chapter we present a unified perspective on the flow-arrest transition spanning the entire range between the thermal and athermal limits. For simplicity, our study focuses on hard-sphere colloidal dispersions. Experiments and simulations at fixed volume (fraction) have found the suspension viscosity to diverge algebraically at a critical volume fraction: $\eta_s \propto (\phi_c - \phi)^{-\delta}$, where ϕ is the volume fraction and δ is the exponent. With strong thermal fluctuations the colloidal glass transition is observed: $\phi_c \approx 0.58$–0.60 and $\delta \approx 2.2$–2.6 [7, 15–17]. In the limit of the jamming transition where thermal fluctuations are weak: $\phi_c \approx 0.585$–0.64 and $\delta \approx 2.0$ [9, 18, 19]. Moreover, ϕ_c is sensitive to the particle size polydispersity [20], particle surface asperity [5], and even the sample preparation protocol [21]. Traditionally, the different exponents are interpreted as signatures of distinct physical processes—the colloidal glass vs. the jamming transition [9]. Here we show that when the suspension pressure, instead of the volume, is held fixed under shear a universal exponent and behavior emerges.

A challenge to dense suspension rheology is the divergence of properties such as viscosity and yield stress near ϕ_c. We overcome this in two ways. First, we impose a constant shear stress rather than shear rate, which allows the system to flow or not, and the yield stress—the stress below which the material does not flow—can be identified. Second, we impose a constant confining pressure rather than a fixed volume, which allows the system to dilate (or compact)—to change its volume fraction—as necessary under flow. In this way we are able to approach the critical point along trajectories at fixed shear stress and pressure, rather than, as is traditional, along paths of fixed shear rate and volume fraction.

It proves revealing to discuss the behavior from a perspective often used in the granular flow community. Although both the shear and normal stresses diverge at the critical point, their ratio does not. For viscous suspensions the behavior can be described in terms of the friction coefficient μ, a *macroscopic*, effective property of the material, and the viscous flow number I_v [19],

$$\mu = \sigma/\Pi \quad \text{and} \quad I_v = \eta_0\dot{\gamma}/\Pi, \tag{6.1}$$

where σ is the shear stress, Π is the particle (or osmotic) pressure, η_0 is the solvent viscosity, and $\dot{\gamma}$ is the strain rate. Using the viscous flow number I_v—the ratio of an internal suspension time scale η_0/Π to the flow time scale $\dot{\gamma}^{-1}$—Boyer *et al.* [19] successfully unified the rheology of viscous non-Brownian suspensions and inertial-driven granular materials.

For rapid granular flows both the shear and normal stresses scale inertially (as $\sim \rho a^2\dot{\gamma}^2$) and their ratio, the friction coefficient, is independent of the strain rate, which has led to the claim that a rate-independent friction coefficient is a signature of (dry) friction-dominated material and flow. However, in viscous non-Brownian suspensions (any colloidal suspension at high shear rates) both σ and Π scale linearly with the strain rate (as $\sim \eta_0\dot{\gamma}$) and the friction coefficient is independent of $\dot{\gamma}$ even though the material behaves as a liquid.

Liquid-like colloidal dispersions are not normally discussed in terms of μ because at low shear rates (strong thermal motion) the shear stress is proportional to $\dot{\gamma}$, but the normal stress is dominated by the equilibrium osmotic pressure and thus $\mu \sim \dot{\gamma}$ as $\dot{\gamma} \to 0$. However, near the flow-arrest point, the material has a dynamic yield stress, and μ may approach a constant as $\dot{\gamma} \to 0$. The friction coefficient perspective therefore enables a natural connection between Brownian suspensions and granular materials.

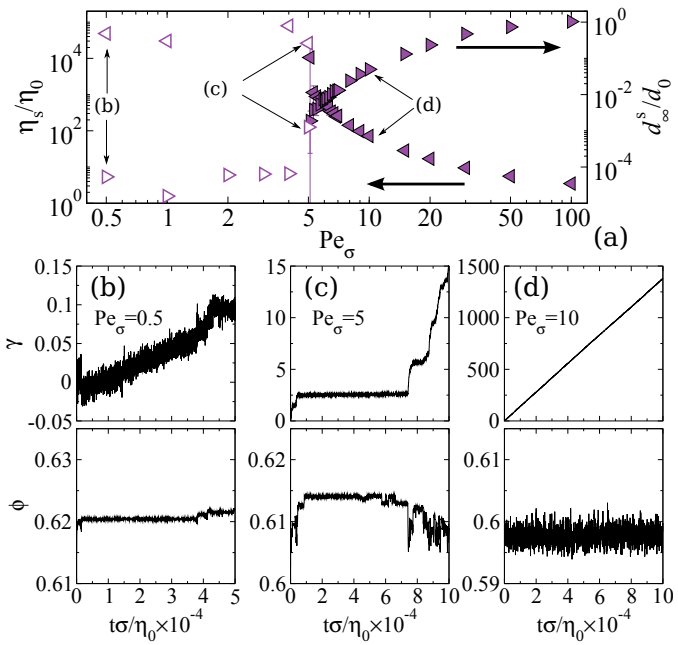

Figure 6.1: (a): The suspension steady shear viscosity η_s/η_0 (left triangles) and the long-time self-diffusivity d^s_∞/d_0 (right triangles), with $d_0 = k_\mathrm{B}T/(6\pi\eta_0 a)$, as functions of Pe_σ in constant shear stress and pressure simulations at an imposed pressure $\Pi a^3/k_\mathrm{B}T = 5$. The filled (open) symbols represent the flowing (arrested) states. Typical accumulated strain γ (top) and volume fraction ϕ (bottom) at Pe_σ = 0.5 (b), 5 (c), and 10 (d) as functions of dimensionless time $t\sigma/\eta_0$ are also presented, with the corresponding Pe_σ annotated in (a).

6.2 Method

We study the suspension rheology using Brownian dynamics (BD) simulations without hydrodynamic interactions (HIs). In the simulations, we enforce the hard-sphere interactions via the 'potential free' algorithm [22–25], and compute ϕ and $\dot\gamma$ from the imposed σ and Π, which, when scaled with the thermal energy $k_\mathrm{B}T$, give, respectively, the stress Péclet number $\mathrm{Pe}_\sigma = 6\pi a^3\sigma/k_\mathrm{B}T$ and the dimensionless pressure $\bar\Pi = \Pi a^3/k_\mathrm{B}T$, with a the mean particle radius. The particle dynamics follow the overdamped Langevin equation,

$$\zeta(\dot{\boldsymbol{x}} - \dot\gamma x_2 \boldsymbol{e}_1 - \tfrac{1}{3}\dot e \boldsymbol{x}) = \boldsymbol{f}_p + \boldsymbol{f}_b, \tag{6.2}$$

where $\boldsymbol{x} = (x_1, x_2, x_3)$ is the particle position in the 1-(velocity), 2-(velocity gradient), and 3-(vorticity) directions, $\zeta = 6\pi\eta_0 a$ is the Stokes resistance, $\dot e$ is the expansion rate, $\boldsymbol{e}_1$ is the unit vector in 1-direction, $\boldsymbol{f}_p$ is the interparticle force [25], and $\boldsymbol{f}_b$ is the Brownian force, which has a mean of zero and a variance of $2k_\mathrm{B}T\zeta$. We impose periodic boundary conditions in 1- and 3-directions and the Lees-Edwards

boundary condition in 2-direction. The strain ($\dot{\gamma}$) and expansion ($\dot{e}$) rates are computed from:

$$\sigma = (1 + \tfrac{5}{2}\phi)\eta_0\dot{\gamma} + \sigma_{12}^p, \tag{6.3}$$

$$\Pi = -(\kappa_0 + \tfrac{4}{3}\phi\eta_0)\dot{e} - \tfrac{1}{3}\boldsymbol{\sigma}^p : \mathbf{I}, \tag{6.4}$$

where κ_0 is the bulk viscosity of the compressible solvent [1], and $\boldsymbol{\sigma}^p = -nk_BT\mathbf{I} - n\left\langle \boldsymbol{x}\boldsymbol{f}_p \right\rangle$ is the particle stress contribution, with $n = N/V$ the number density. The simulation box size L is then adjusted isotropically as $\dot{L} = \frac{1}{3}\dot{e}L$. The novelty of our method is that, through a compressible solvent, the constant pressure constraint for the overdamped system is satisfied without introducing permeable boundaries.

For each $(\mathrm{Pe}_\sigma, \bar{\Pi})$ pair we perform at least three independent simulations, each contains $N = 200$ particles with 10% particle size polydispersity [8]. The simulation lasts at least 10^4 dimensionless time units with step size 10^{-4}, where the time is scaled with $6\pi\eta_0 a^3/k_BT$ when $\mathrm{Pe}_\sigma < 1$ and with η_0/σ when $\mathrm{Pe}_\sigma \geq 1$. In the appendices, we describe the computation of $\boldsymbol{f}_p$, and show that the selected parameters adequately capture the physics of flow-arrest transitions.

6.3 Results and discussions

Typical rheological responses from constant stress and pressure simulations at an imposed pressure $\bar{\Pi} = 5$ are shown in Fig. 6.1. The Pe_σ dependence of the shear viscosity $\eta_s = \sigma/\dot{\gamma}$ and the long-time self-diffusivity (LTSD) d_∞^s, measured from the slope of the mean-square displacement in the vorticity direction, $d_\infty^s = \lim_{t\to\infty} \frac{1}{2}\mathrm{d}\langle(\Delta x_3)^2\rangle/\mathrm{d}t$, are presented in Fig. 6.1a. The suspension exhibits a flow-arrest transition at $\mathrm{Pe}_\sigma \approx 5$, with the flowing data shown as filled symbols and the arrested data as open symbols. When $\mathrm{Pe}_\sigma \gtrsim 5$, the shear viscosity increases sharply with decreasing Pe_σ, reaching $\eta_s/\eta_0 \approx 2 \times 10^4$ at $\mathrm{Pe}_\sigma \approx 5$. Accompanying the growth in η_s is an abrupt reduction in d_∞^s. At lower Pe_σ, the shear viscosity remains high and the LTSD low. Fig. 6.1b–6.1d show behaviors of the accumulated strain $\gamma = \int_0^t \dot{\gamma}\mathrm{d}t$ and the volume fraction ϕ at different Pe_σ. The accumulated strain grows linearly with time in the flowing state, but changes little in the arrested state. At $\mathrm{Pe}_\sigma = 5$ in Fig. 6.1c, γ exhibits instability and switches between the flowing and arrested states. Correspondingly, ϕ fluctuates around a mean value for both the flowing and arrested suspensions, but becomes unstable at the flow-arrest point. We

[1] Treating the solvent as a compressible fluid allows the periodic unit cell to be expanded isotropically without violating the physics of Brownian particles in Stokes flow, c.f. Ref. [26]. Thus, a physical permeable boundary, which can cause local ordering, etc., is not necessary.

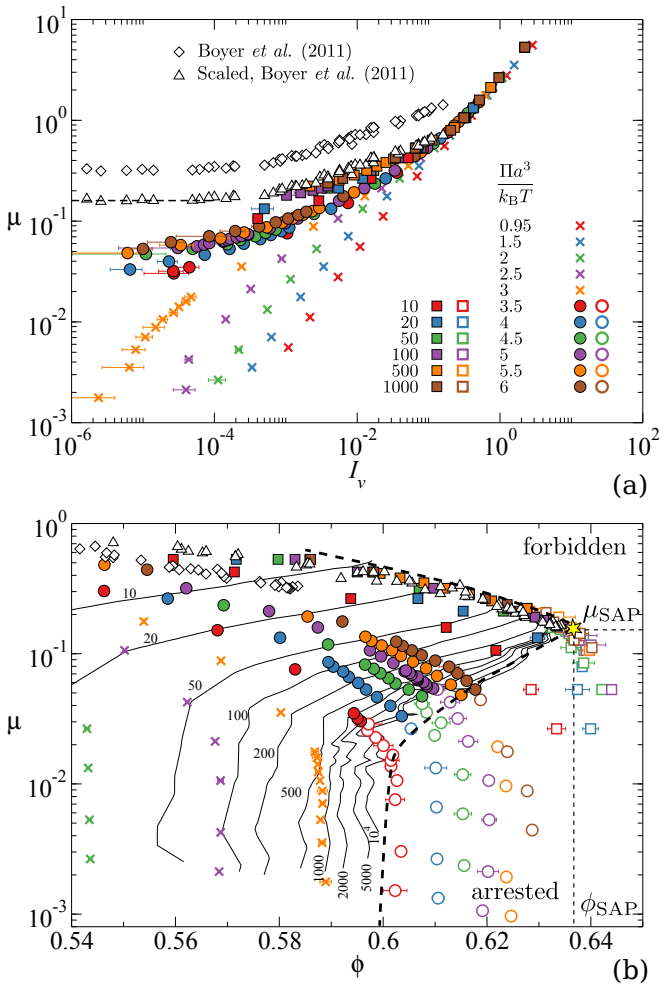

Figure 6.2: (Color online) The steady shear rheology of hard-sphere colloidal suspensions with constant shear stress and pressure, (a): $\mu = \sigma/\Pi$ as a function of $I_v = \eta_0\dot{\gamma}/\Pi$ and (b): μ as a function of ϕ. Simulations at the same imposed pressure $\Pi a^3/k_BT$ are shown in the same symbols. For suspensions exhibiting flow-arrest transitions, the filled (open) symbols represent the flowing (arrested) states. The raw and the scaled data of Boyer *et al.* [19] are shown in diamonds and triangles, respectively. In (b), the dashed lines outline the boundary of the flowing region, and the solid lines are contours of the shear viscosity η_s/η_0. The *Shear Arrest Point* (ϕ_{SAP}, μ_{SAP}) is shown as a star.

found that the suspensions is arrested when $\eta_s/\eta_0 > 2 \times 10^4$ over a wide range of imposed pressures. Consequently, this is adopted as a criterion for the flow-arrest transition in this work.

Fig. 6.2 presents the overall steady shear rheology at constant stress and pressure near the flow-arrest transition. Fig. 6.2a shows the friction coefficient as a function

of the viscous number, and Fig. 6.2b shows the corresponding volume fraction. The symbols of the same color are at the same confining pressure (shown in the figure legend) and trace out 'isobars'. Full symbols are flowing liquid-like systems, while unfilled symbols denote arrested states.

Starting with solid ×'s at low confining pressures, *e.g.*, at $\bar{\Pi} = 0.95$ in Fig. 6.2a, μ grows linearly with I_v at low and high I_v with different slopes; the suspension does not arrest. The ratio of μ and I_v is the shear viscosity, $\eta_s/\eta_0 = \mu/I_v$. At high I_v, the suspension viscosity η_s asymtotes to the solvent viscosity η_0. With increasing $\bar{\Pi}$, the μ-I_v curve flattens as I_v decreases, but eventually turns down such that $\mu \sim \dot{\gamma}$ as $\dot{\gamma} \to 0$. The suspension flows as a liquid with an increasing zero shear-rate viscosity corresponding to the larger ϕ seen in Fig. 6.2b.

When the confining pressure $\bar{\Pi} \geq 3.5$, the suspension arrests and flows only if μ exceeds a limiting value $\mu_m(\bar{\Pi})$, and the minimum shear rate (I_v) increases. The imposed stress corresponding to μ_m is the dynamic yield stress at the imposed pressure. Moreover, μ_m increases with $\bar{\Pi}$ and, as $\bar{\Pi} \to \infty$, μ_m asymptotes to a constant value of 0.16. At high $\bar{\Pi}$ (and high I_v for low $\bar{\Pi}$) all data collapse onto a single curve corresponding to the limiting behavior of non-Brownian viscous suspensions.

Fig. 6.2b shows the corresponding μ-ϕ curves. At low confining pressures (the ×'s) the volume fraction increases as the shear stress (μ) decreases. When arrested, $\bar{\Pi} \geq 3.5$ (open symbols), dilation always precedes flow as the shear stress is increased and the maximum flowable volume fraction ϕ_m is always lower than the zero-shear value. As a point of reference, the zero-shear volume fraction at $\bar{\Pi} = 3.5$ is $\phi = 0.60$ for our system. As $\bar{\Pi} \to \infty$, ϕ_m asymptotes to a constant value and the non-Brownian limit emerges as the μ-ϕ curves collapse. The flowing region in Fig. 6.2b is bounded from below by the arrested region and from above by the non-Brownian behavior.

The rightmost point of the flowing region, highlighted as a star in Fig. 6.2b, corresponds to the flow-arrest transition in the viscous non-Brownian limit. This point is referred to as the *Shear Arrest Point* (SAP):

$$(\phi_{\mathrm{SAP}}, \mu_{\mathrm{SAP}}) = \lim_{\bar{\Pi}\to\infty} (\phi_m, \mu_m) \approx (0.635, 0.16)\,, \tag{6.5}$$

which represents a limit beyond which the suspension is unable to flow regardless of the imposed pressure and shear stress. The SAP is uniquely determined from the constant stress and pressure rheology protocol and therefore may differ from other

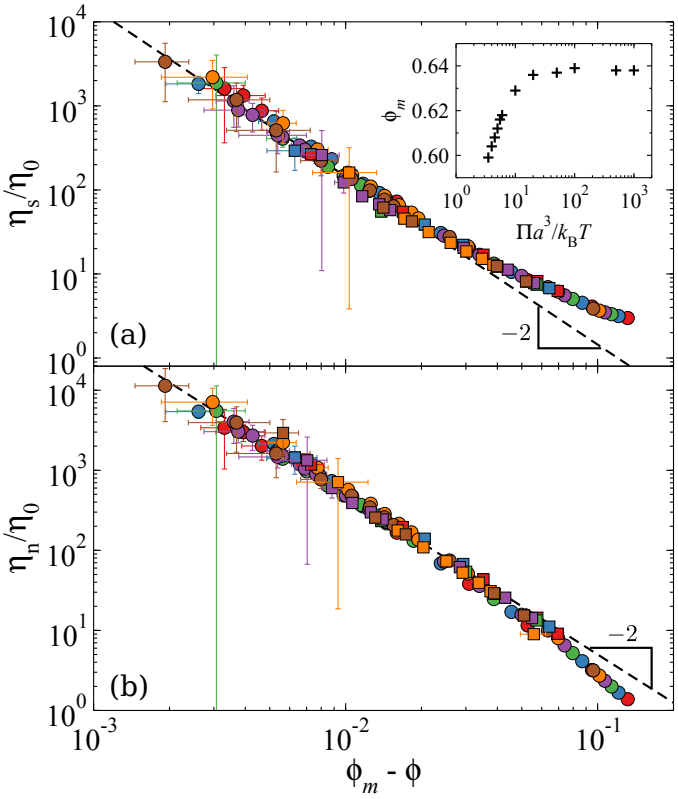

Figure 6.3: (Color online) Universal viscosity divergences (a): the shear viscosity η_s/η_0 and (b): the incremental normal viscosity η_n/η_0 as functions of $(\phi_m - \phi)$, the volume fraction difference from arrest, for flowing suspensions with $\bar{\Pi} \geq 3.5$. The inset of (a) shows ϕ_m as a function of $\bar{\Pi}$. The legends are identical to those in Fig. 6.2.

'jamming' points [5, 6]. In fact, ϕ_{SAP} is lower than the maximum random jammed (MRJ) density of the corresponding polydisperse packing $\phi_{\mathrm{MRJ}} \approx 0.645$.

Also presented in Fig. 6.2b are the shear viscosity contours up to $\eta_s/\eta_0 = 10^4$. Horizontal traversal near $\mu = 0$ recovers the equilibrium suspension behavior near the glass transition. The viscosity diverges at $\phi_g \approx 0.6$, which is also found experimentally in similar systems [16, 17, 27]. Vertical crossing corresponds to the constant volume rheology and the viscosity exhibits shear-thinning. Near the SAP, the range of μ in the flowing region reduces drastically for constant volume rheology. On the other hand, constant stress and pressure rheology allows the suspension to dilate and to find the SAP dynamically, a key merit of our approach.

In the flowing region near the flow-arrest transition both the shear viscosity η_s and the incremental normal viscosity η_n diverge as shown in Fig. 6.3. The incremental

normal viscosity η_n characterizes the flow contribution to the osmotic pressure,

$$\eta_n = (\Pi - \Pi^{eq})/\dot{\gamma}, \tag{6.6}$$

where Π^{eq} is the zero-shear equilibrium osmotic pressure at the same volume fraction. Both η_s and η_n diverge algebraically when approaching the flow-arrest transition: $(\eta_s, \eta_n) \sim (\phi_m - \phi)^{-2}$; the exponent 2 is independent of the imposed pressure and thus valid for both strong and weak thermal fluctuations. The same viscosity divergence exponents were found in experiments [19] and simulations [28] of non-Brownian systems, suggesting the physics of jamming is the most important and universal aspect of the flow-arrest transition. Thermal fluctuations only affect the arrest volume fraction ϕ_m, as shown in the inset of Fig. 6.3a.

Note that the divergence of the shear viscosity with an exponent of 2 is not inconsistent with exponent 2.2–2.6 reported for the colloidal glass transition. For the glass transition, one approaches the arrested region in Fig. 6.2b horizontally by varying the volume fraction at low μ, whereas the divergences observed here are for approaching arrest at fixed pressure. Both where the viscosity starts to diverge, ϕ_m, and how steep is the rise, the exponent α, depend on how the 'mountain' (the viscosity contours) is approached.

The data collapse in Fig. 6.3 can be explained by the internal structural relaxations in colloidal dispersions. The inherent relaxation from thermal fluctuations is characterized by $d_\infty^{s,0}$, and for glassy materials $\phi > \phi_g$, $d_\infty^{s,0} \to 0$. Comparing the shear to the inherent Brownian forces defines a zero-shear Péclet number $\dot{\gamma}a^2/d_\infty^{s,0}$ and shows that, in the glassy or arrested state, any finite shear rate gives a *large* Péclet number. The system is driven far from equilibrium and therefore shows universal behaviors. Indeed, this is seen in η_n: linear response would dictate that $\eta_n \propto \dot{\gamma}$ as $\dot{\gamma} \to 0$ [29], rather than be independent of $\dot{\gamma}$ as seen in Fig. 6.3b. There is no linear response regime near a flow-arrest point. This may explain why the inherently non-equilibrium isobaric flow-arrest transition of colloidal dispersions has features in common with the athermal granular jamming transitions [30–32].

Finally, we compare our simulations to the experiments of Boyer *et al.* [19], whose results are shown as diamonds in Fig. 6.2. The experimental data qualitatively agree with the simulation results in the non-Brownian limit ($\bar{\Pi} \to \infty$); however, their flow-arrest critical point $(\phi_c, \mu_c) = (0.585, 0.32)$ is quite different. We can achieve quantitative agreement by scaling the experimental data from (ϕ, μ) to (ϕ', μ') as

$$\frac{\mu'}{\mu} = \frac{\phi_{\mathrm{SAP}} - \phi'}{\phi_c - \phi} = \frac{\mu_{\mathrm{SAP}}}{\mu_c}, \tag{6.7}$$

which are shown as triangles in Fig. 6.2 and match the simulation results. The scaling of Eq. (6.7) implies that the fundamental physics behind the viscous non-Brownian arrest does not change with the HIs or the possible frictional contact forces in the experiments. Our simulations clearly capture the physics of the flow-arrest transition.

That $\mu_c > \mu_{\mathrm{SAP}}$ can be understood from the lack of HIs in the simulations. Hydrodynamics give an additional contribution to the shear stress via the high-frequency dynamic viscosity, which increases σ and therefore μ. However, they do not explain the difference in the computational ϕ_{SAP} and the experimental ϕ_c seen in Fig. 6.2b. One interpretation is that frictional contact forces in the experiments reduce the arrest volume fraction [5, 12]. Yet, there is a simpler explanation. In the experiments near suspension arrest, the minimum suspension height in the shear cell (8.8 mm) is not much larger than the particle diameter (1.1 mm) [19, 33]. There is a region of order the particle size a adjacent to the apparatus walls that is inaccessible to the particles. Using the accessible volume rather than the total volume can increase the volume fraction by as much as 11% and account for the difference between ϕ_{SAP} and ϕ_c. Clearly, extreme care is needed when studying dense suspensions as seemingly unimportant details can drastically affect the results.

6.4 Conclusions

This chapter demonstrates that constant stress and pressure rheology is an effective approach to study the flow-arrest transitions of dense amorphous materials and provides a unique perspective to distinguish the most fundamental physics in this transition. We found the viscous non-Brownian *Shear Arrest Point* (SAP) of hard-sphere colloidal suspensions from the collapse of the flow curves. The results strongly suggest that the jamming and glass transitions are different facets of the same phenomenon, offering the hope for a unified understanding.

6.A Computing the interparticle force

In BD the overdamped Langevin equation [Eq. (6.2)] is integrated with respect to time. Since the interactions in hard-sphere suspensions are singular, particle overlap is unavoidable regardless of the step size Δt. In the 'potential free' algorithm, the overlap-free condition is maintained in a predictor-corrector fashion: in the predictor step, the dynamics are evolved without the hard-sphere potential, and in the corrector step, the algorithm checks the particle overlap that violates the hard-sphere potential and moves the overlapping particles back to contact pairwise along the line that

connects the particle centers until the suspension is overlap-free. If particle i at $\boldsymbol{r}_i$ overlaps particle j at $\boldsymbol{r}_j$, *i.e.*, $|\boldsymbol{r}_{ij}| > (a_i + a_j)$, where $\boldsymbol{r}_{ij} = \boldsymbol{r}_i - \boldsymbol{r}_j$ and a_i and a_j are the particle radii, the particles are moved along $\boldsymbol{r}_{ij}$ according to

$$\Delta\boldsymbol{r}_i = a_j\boldsymbol{\Delta}_{ij} \text{ and } \Delta\boldsymbol{r}_j = -a_i\boldsymbol{\Delta}_{ij}, \tag{6.8}$$

where $\boldsymbol{\Delta}_{ij} = \boldsymbol{r}_{ij}[|\boldsymbol{r}_{ij}|^{-1} - (a_i + a_j)^{-1}]$. The interparticle force on particle i is computed according to Stokes law,

$$\boldsymbol{f}_{p,i} = 6\pi\eta_0 a_i \Delta\boldsymbol{r}_i/\Delta t, \tag{6.9}$$

and here the Newton's third law is satisfied $\boldsymbol{f}_{p,i} + \boldsymbol{f}_{p,j} = 0$.

6.B System size dependence

Fig. 6.4 presents the system size dependence on the suspension shear viscosity η_s, the long-time self-diffusivity d^s_∞, and the maximum of the dynamic susceptibility $\max(\chi_4)$ as functions of Pe_σ with different system sizes N. The imposed pressure is $\bar{\Pi} = 5$. The dynamic susceptibility χ_4 for an N-particle system is defined as [34],

$$\chi_4(\boldsymbol{k}, t) = N[\langle F_s(\boldsymbol{k}, t)^2\rangle - \langle F_s(\boldsymbol{k}, t)\rangle^2], \tag{6.10}$$

where $F_s(\boldsymbol{k}, t) = N^{-1}\sum_i e^{\imath\boldsymbol{k}\cdot[\boldsymbol{x}_i(t) - \boldsymbol{x}_i(0)]}$ is the self-intermediate scattering function, $\boldsymbol{k}$ is the wave vector, $\imath = \sqrt{-1}$, and $\boldsymbol{x}_i(t)$ is the particle position at time t. In Fig. 6.4c the wave vector $\boldsymbol{k}$ is in the vorticity direction and $|\boldsymbol{k}|a = 3.72$, near the first peak of the static structure factor. When $\mathrm{Pe}_\sigma > 5$, η_s/η_0, d^s_∞/d_0, and $\max(\chi_4)$ show little N-dependence for flowing suspensions. Near the flow-arrest transition, there are quantitative differences at different N. For example, with increasing N, the Pe_σ corresponding to the flow-arrest point shifts slightly towards lower Pe_σ, and the suspensions can achieve higher $\max(\chi_4)$ and lower d^s_∞. However, the qualitative behaviors in Fig. 6.4 remain consistent. Using a modest system size of $N = 200$ captures the physics behind the flow-arrest transition with only small quantitative differences in the $N \to \infty$ limit, and allows us to explore a wide range of parameters in a reasonable amount of time.

6.C Initial condition dependence

To investigate the effect of initial conditions on the BD simulation results, we performed simulations at $N = 200$ for a few $(\bar{\Pi}, \mathrm{Pe}_\sigma)$ pairs near the flow-arrest transitions. Each $(\bar{\Pi}, \mathrm{Pe}_\sigma)$ pair corresponds to 50 independent runs with distinct initial configurations generated from the Lubachevsky-Stillinger algorithm [35], which is also used in this work. Each run lasts 5×10^3 dimensionless time units

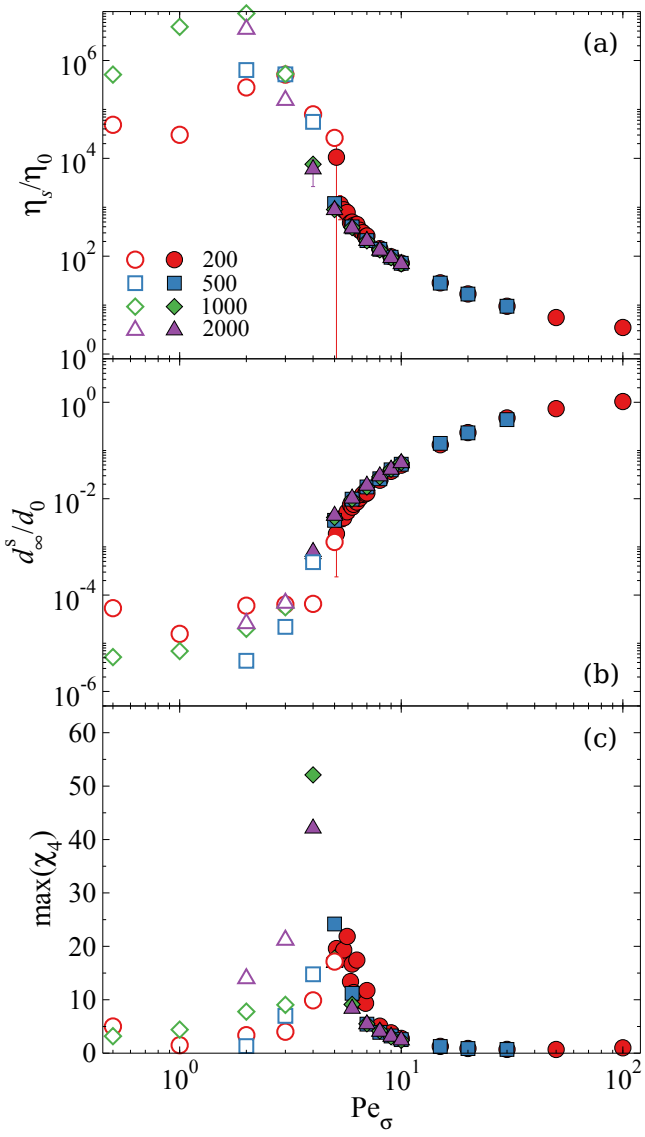

Figure 6.4: (Color online) The system size dependence on (a): the suspension shear viscosity η_s/η_0, (b): the long-time self-diffusivity d^s_∞/d_0. and (c): the maximum of the dynamic susceptibility max(χ_4) as functions of Pe_σ for constant stress and pressure simulations at $\Pi a^3/k_BT = 5$. The filled (open) symbols represent the flowing (arrested) suspension states.

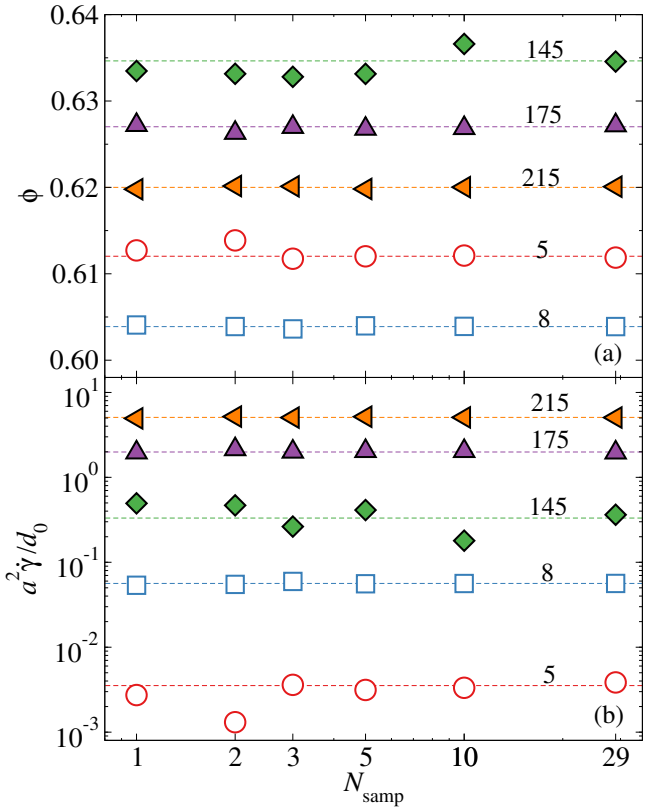

Figure 6.5: (Color online) The initial condition dependence on (a): the average volume fraction ϕ and (b): the average strain rate $\dot{\gamma}a^2/d_0$, with $d_0 = k_{\mathrm{B}}T/(6\pi\eta_0 a)$, as functions of the number of independent simulations in the group N_{samp}. The simulations are performed at $\Pi a^3/k_{\mathrm{B}}T = 5$ (open symbols) and 50 (filled symbols). The stress Péclet number Pe_σ are annotated in on the graph. The dashed lines show the overall average of all 50 independent runs.

with a step size 10^{-3}. Further decreasing the step size to the value used in this work (10^{-4}) does not alter the results. To quantify the initial condition dependence, we randomly partitioned the results to independent groups of $N_{\mathrm{samp}} = 1$, 2, 3, 5, 10, and 29 runs and compute the group average of the volume fraction ϕ and the scaled strain rate $a^2\dot{\gamma}/d_0$ (after the initial transient). Fig. 6.5 presents the results at $\bar{\Pi} = 5$ (open symbols) and 50 (filled symbols), representing the behaviors at low and high imposed pressures, as functions of the group size N_{samp}. The average from the entire 50 runs are shown dashed lines in the corresponding color. For reference, the flow-arrest transition takes place at $\mathrm{Pe}_\sigma \approx 5$ for $\bar{\Pi} = 5$ and $\mathrm{Pe}_\sigma \approx 130$ for $\bar{\Pi} = 50$.

Fig. 6.5 shows the group size N_{samp} does not affect the average ϕ and $\dot{\gamma}$ when Pe_σ is higher than the yield Péclet number. Here, the suspension flows as liquid and the

thermal and mechanical fluctuations erase any influences of the initial conditions. However, close to the flow-arrest transitions, *i.e.*, $(\bar{\Pi}, \mathrm{Pe}_\sigma) = (50, 145)$ and $(5, 5)$, the results are more sensitive to N_{samp}: both ϕ and $\dot{\gamma}$ fluctuates around the mean value without a definite trend. This fluctuation is also reflected in the large error bars in Fig. 6.3. Fig. 6.5 further demonstrates that $N_{\mathrm{samp}} \geq 3$ adequately reflects the system behavior and justifies the computational protocol of this work. It also validates that our results and conclusions are independent of the initial conditions.

References

[1] N. J. Wagner and J. F. Brady, "Shear thickening in colloidal dispersions", Phys. Today **62**, 27 (2009).

[2] J. F. Morris and F. Boulay, "Curvilinear flows of noncolloidal suspensions: the role of normal stresses", J. Rheo. **43**, 1213 (1999).

[3] F. Varnik, L. Bocquet, J.-L. Barrat, and L. Berthier, "Shear localization in a model glass", Phys. Rev. Lett. **90**, 095702 (2003).

[4] A. J. Liu and S. R. Nagel, "Nonlinear dynamics: jamming is not just cool any more", Nature **396**, 21 (1998).

[5] D. Bi, J. Zhang, B. Chakraborty, and R. P. Behringer, "Jamming by shear", Nature **480**, 355 (2011).

[6] T. K. Haxton, M. Schmiedeberg, and A. J. Liu, "Universal jamming phase diagram in the hard-sphere limit", Phys. Rev. E **83**, 031503 (2011).

[7] A. Ikeda, L. Berthier, and P. Sollich, "Unified study of glass and jamming rheology in soft particle systems", Phys. Rev. Lett. **109**, 018301 (2012).

[8] N. Koumakis, M. Laurati, S. U. Egelhaaf, J. F. Brady, and G. Petekidis, "Yielding of hard-sphere glasses during start-up shear", Phys. Rev. Lett. **108**, 098303 (2012).

[9] A. Ikeda, L. Berthier, and P. Sollich, "Disentangling glass and jamming physics in the rheology of soft materials", Soft Matter **9**, 7669 (2013).

[10] P. Olsson and S. Teitel, "Athermal jamming versus thermalized glassiness in sheared frictionless particles", Phys. Rev. E **88**, 010301(R) (2013).

[11] N. Estrada, E. Aźema, F. Radjai, and A. Taboada, "Identification of rolling resistance as a shape parameter in sheared granular media", Phys. Rev. E **84**, 011306 (2011).

[12] R. Seto, R. Mari, J. F. Morris, and M. M. Denn, "Discontinuous shear thickening of frfriction hard-sphere suspensions", Phys. Rev. Lett. **111**, 218301 (2013).

[13] R. Mari, R. Seto, J. F. Morris, and M. M. Denn, "Discontinuous shear thickening in brownian suspensions by dynamic simulation", arXiv: 1508.01243 (2015).

[14] C. Heussinger, "Shear thickening in granular suspensions: interparticle friction and dynamically correlated clusters", Phys. Rev. E **88**, 050201(R) (2013).

[15] W. van Megen, T. C. Mortensen, S. R. Williams, and J. Müller, "Measurement of the self-intermediate scattering function of suspensions of hard spherical particles near the glass transition", Phys. Rev. E **58**, 6073 (1998).

[16] G. Brambilla, D. El Masri, M. Pierno, L. Berthier, L. Cipelletti, G. Petekidis, and A. Schofield, "Probing the equilibrium dynamics of colloidal hard spheres above the mode-coupling glass transition", Phys. Rev. Lett. **102**, 085703 (2009).

[17] J. Reinhardt, F. Weysser, and M. Fuchs, "Comment on "probing the equilibrium dynamics of colloidal hard spheres above the mode-coupling glass transition"", Phys. Rev. Lett. **105**, 199604 (2010).

[18] W. B. Russel, N. J. Wagner, and J. Mewis, "Divergence in the low shear viscosity for brownian hard sphere dispersions: at random close packing or the glass transition?", J. Rheo. **57**, 1555 (2013).

[19] F. Boyer, E. Guazzelli, and O. Pouliquen, "Unifying suspension and granular rheology", Phys. Rev. Lett. **107**, 188301 (2011).

[20] W. C. K. Poon, E. R. Weeks, and C. P. Royall, "On measuring colloidal volume fractions", Soft Matter **8**, 21 (2012).

[21] P. Chaudhuri, L. Berthier, and S. Sastry, "Jamming transitions in amorphous packings of frictionless spheres occur over a continuous range of volume fractions", Phys. Rev. Lett. **104**, 165701 (2010).

[22] D. M. Heyes and J. R. Melrose, "Brownian dynamics simulations of model hard-sphere suspensions", J. Non-Newtonian Fluid Mech. **46**, 1 (1993).

[23] W. Schaertl and H. Sillescu, "Brownian dynamics simulations of colloidal hard spheres. effects of sample dimensionality on self-diffusion", J. Stat. Phys. **74**, 687 (1994).

[24] P. Strating, "Brownian dynamics simulation of a hard-sphere suspension", Phys. Rev. E **59**, 2175 (1999).

[25] D. R. Foss and J. F. Brady, "Brownian dynamics simulation of hard-sphere colloidal dispersions", J. Rheo. **44**, 629 (2000).

[26] J. F. Brady, A. S. Khair, and M. Swaroop, "On the bulk viscosity of suspensions", J. Fluid Mech. **554**, 109 (2006).

[27] D. El Masri, G. Brambilla, M. Pierno, G. Petekidis, A. Schofield, L. Berthier, and L. Cipelletti, "Dynamic light scattering measurements in the activated regime of dense colloidal hard spheres", J. Stat. Mech. Theor. Exp. **2009**, P07015 (2009).

[28] M. Trulsson, B. Andreotti, and P. Claudin, "Transition from the viscous to inertial regime in dense suspensions", Phys. Rev. Lett. **109**, 118305 (2012).

[29] J. F. Brady and M. Vicic, "Normal stresses in colloidal dispersions", J. Rheo. **39**, 545 (1995).

[30] E. Lerner, G. Düring, and M. Wyart, "A unified framework for non-brownian suspension flows and soft amorphous solids", Proc. Natl. Acad. Sci. USA **109**, 4798 (2012).

[31] M. Bouzid, M. Trulsson, P. Claudin, E. Clément, and B. Andreotti, "Nonlocal rheology of granular flows across yield conditions", Phys. Rev. Lett. **111**, 238301 (2013).

[32] B. Andreotti, J.-L. Barrat, and C. Heussinger, "Shear flow of non-brownian suspensions close to jamming", Phys. Rev. Lett. **109**, 105901 (2012).

[33] F. Boyer, "Suspensions concentrées : expériences originales de rhéologie", PhD thesis (Aix-Marseille Université, 2011).

[34] C. Toninelli, M. Wyart, L. Berthier, G. Biroli, and J.-P. Bouchaud, "Dynamical susceptibility of glass formers: contrasting the predictions of theoretical scenarios", Phys. Rev. E **71**, 041505 (2005).

[35] B. D. Lubachevsky and F. H. Stillinger, "Geometric properties of random disk packings", J. Stat. Phys. **60**, 561 (1990).